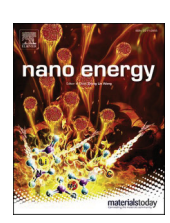


Contents lists available at ScienceDirect

Nano Energy

journal homepage: www.elsevier.com/locate/nanoen





Interstitial carbon atoms enhance both selectivity and activity of rhodium catalysts toward C-C cleavage in direct ethanol fuel cells

Zhenming Cao ^{a,b,1}, Huiqi Li ^{a,1}, Qiyuan Fan ^{a,1}, Zhantao Liu ^d, Zitao Chen ^{b,c}, Yunchao Sun ^a, Jinyu Ye ^a, Maofeng Cao ^a, Cong Shen ^a, Yaqi Jiang ^a, Miaofang Chi ^c, Jun Cheng ^{a,*}, Hailong Chen ^{d,*}, Zhaoxiong Xie ^{a,*}, Younan Xia ^b

- ^a State Key Laboratory of Physical Chemistry of Solid Surfaces, IKKEM, Collaborative Innovation Center of Chemistry for Energy Materials, College of Chemistry and Chemical Engineering, Xiamen University, Xiamen, Fujian 361005, China
- b The Wallace H. Coulter Department of Biomedical Engineering, Georgia Institute of Technology and Emory University, Atlanta, GA 30332, United States
- ^c Center for Nanophase Materials Sciences, Oak Ridge National Laboratory, Oak Ridge, TN 37831, United States
- ^d The Woodruff School of Mechanical Engineering, Georgia Institute of Technology, Atlanta, GA 30332, United States

ARTICLEINFO

Keywords: Interstitial carbon atom Rhodium catalyst C-C cleavage Selectivity Direct ethanol fuel cells

ABSTRACT

Selective breaking of the C-C bond in ethanol holds the key to many industrial processes, including the operation of direct ethanol fuel cells and steam reforming. Interstitial C atoms in the subsurface region of noble-metal catalysts have major impacts on the selectivity and activity, but an understanding of the mechanistic details is still elusive due to their nature of in situ formation and metastability. Herein, we develop a method to obtain stable RhC_x (x \approx 0.5) by introducing C atoms into the interstitial sites of well-defined Rh nanosheets of 8–10 at layers in thickness, and further elucidate the electronic and geometric effects of the interstitial C atoms on the cleavage of C-C bond. With the introduction of C atoms into half of the octahedral sites, the Rh lattice changes from a cubic to an orthorhombic structure. The lattice expansion induced by the insertion of C atoms, together with the electron transfer between C and Rh atoms, effectively suppresses the coupling reaction between OH* and CH₃CO* to form acetic acid while making the cleavage of C-C bond more exothermic. As such, we obtain a selectivity of ethanol to CO₂ as high as 18.1 %, much higher than those of the Rh counterpart (10.0 %), together with 3.1-fold improvement in kinetics. Guided by these findings, a new method is also developed to directly introduce C atoms into the subsurface of a commercial Rh black to enhance its selectivity and activity by 2.5- and 1.6- folds, respectively.

1. Introduction

Noble-metal nanocrystals have found extensive use as heterogeneous catalysts in industrial processes, including those pivotal to fine chemical [1,2], pharmaceutical [3], energy conversion [4,5], and environmental protection [6]. In all these applications, it is critical to optimize both selectivity and activity of the catalysts. Regulating the interactions of the reactant/intermediates to the catalyst at the atomic level is the principal strategy to selectively acquire the desired products at a high efficiency [7,8]. To this end, controlling the size and shape of nanocrystals in terms of surface atomic structures (e.g., the types and fractions of atomic terraces, steps, and kinks) offers an effective mean to tailor the interactions between reactant/intermediates and a metal surface [9]. The

electron transfer from other synergistic components, such as alloys, supports and organic modifiers can also be leveraged to modulate the chemisorption energy of reaction intermediates [10–15]. Compared with the aforementioned synergistic components, light nonmetal elements such as H, B, C, N, P can be introduced into the interstitial sites of noble metals to tune the catalytic properties through lattice variation (including symmetry and strain), charge transfer as well as orbital hybridizations [16]. Among these interstitial metallic compounds, noble metal borides are the most popular materials due to the mild synthesis conditions, and the corresponding structures and electrochemical properties are also extensively investigated [17]. In contrast, studies about the noble metal carbides, especially for the electrocatalysis, are relatively fewer, since C atoms are usually considered detrimental to the

^{*} Corresponding authors.

E-mail addresses: chengjun@xmu.edu.cn (J. Cheng), hailong.chen@me.gatech.edu (H. Chen), zxxie@xmu.edu.cn (Z. Xie).

¹ These authors contributed equally to this work.

performance of noble metal catalysts, as exemplified by the undesired coking process [18]. However, recent studies indicate that interstitial C atoms in the subsurface can enhance catalytic activity and/or selectivity toward various industrially important reactions [19,20]. It is anticipated that lattice C atoms hold promise to alleviate the current issues facing many industrial catalysts [21-23]. Unfortunately, the carbides of noble metals are mainly formed in situ under stringent conditions that critically depend on the use of a high temperature and/or pressure, a specific component of the reactive gas, as well as some specific sites such as corners and atomic steps of one to a few atomic layers [24-27]. Such requirements make it challenging to elucidate the intrinsic structure and the effects of lattice C atoms on catalytic selectivity. Although some efforts on the synthesis of noble metal carbides have been made, it is still difficult to achieve an atomic-level picture about the carbide phase and the related surface events during the catalytic process due to the metastability and/or ambiguous surface structure of the prepared carbides [28,29].

Direct ethanol fuel cells (DEFCs) are one of the most promising energy conversion devices, but their development is still impeded by the inefficient oxidation of ethanol on the anode catalysts due to the poor performance in C-C bond cleavage [30–35]. To achieve a higher selectivity, the surface structure of the catalysts, including the atomic arrangements and compositions, is supposed to be appropriately tailored to facilitate both the C-C bond cleavage and the subsequent formation of

 ${\rm CO}_2$. Besides, bifunctional effect to accelerate the removal of CO and ${\rm CH}_{\rm x}$ species with the assistance of ${\rm OH}_{\rm ads}$ is another key point to be considered for better activity [36–39]. Therefore, great efforts and improvement have been made in this field, but there is still a long way off for the large-scale commercialization of DEFCs.

Herein, we report a mild synthesis of stable well-defined RhC_x nanosheets with half of the lattice octahedral sites being occupied by C atoms, where the Rh lattice changes from the highly symmetric face-centered cubic to an orthorhombic structure. With the specific surface structures as well as well-controlled interstitial C atoms, the relations between the intercalated C atoms in Rh catalysts and the corresponding properties for the selective cleavage of C-C bond in ethanol are clearly elucidated at the molecular level. More importantly, same method has also been extended to introduce C atoms into the subsurface of commercial Rh black to enhance its catalytic performance, which shows a good prospect for industrial applications.

2. Results and discussion

2.1. Synthesis and structural characterizations of RhC_x nanosheets

We obtained the RhC_x phase by reducing $Rh(acac)_3$ in a mixture of formaldehyde and oleylamine. As shown by the TEM image in Fig. 1a, the as-obtained RhC_x adopted a flower-like morphology, consisting of

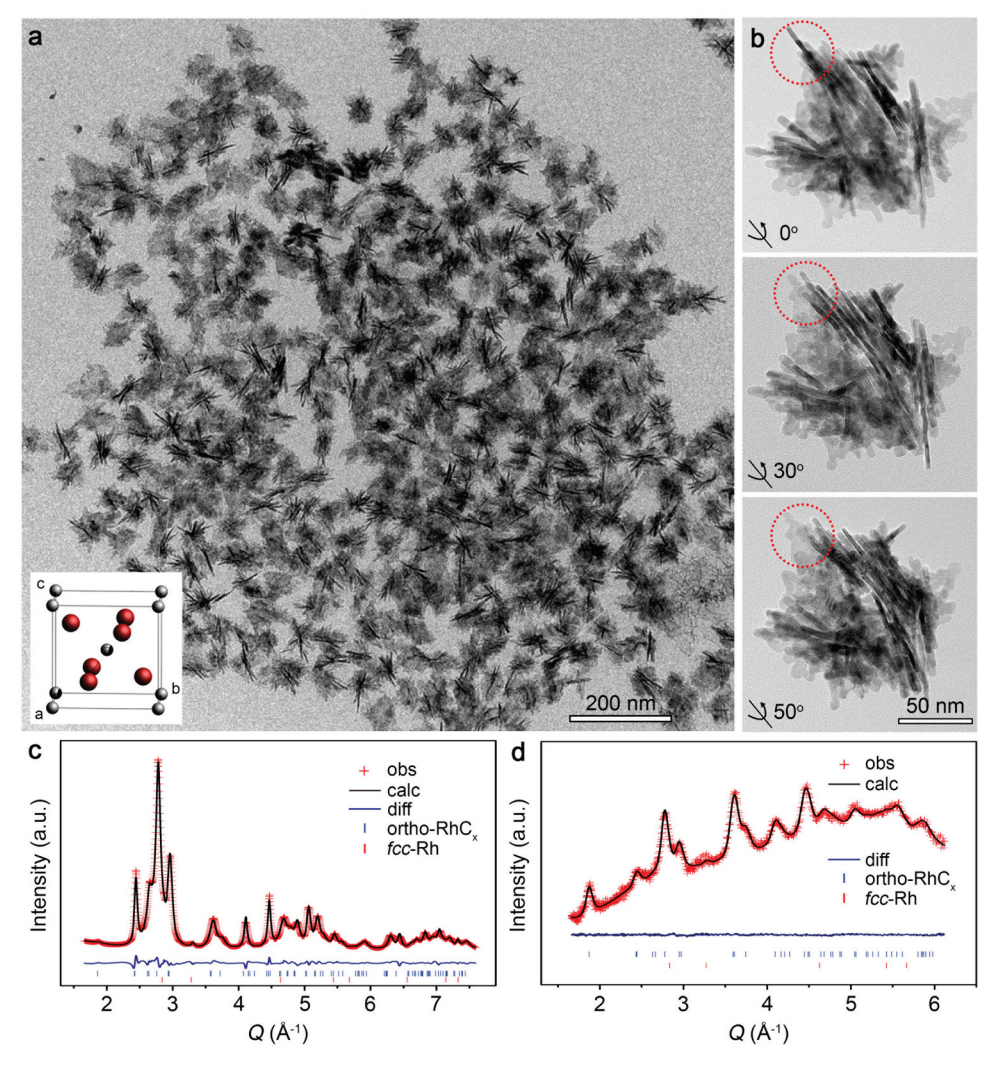


Fig. 1. (a) TEM image of the as-prepared sample, with the inset showing the unit cell of the RhC_x phase. (b) TEM images recorded from the same area at different tilting angles. (c) and (d), Comparison between the diffraction patterns recorded experimentally and calculated using *Rietveld* refinement with an orthorhombic structure model, and their difference for (c) X-ray and (d) neutron diffraction, respectively.

loosely stacked nanosheets with average lateral dimensions of 100 ± 20 nm. Fig. 1b shows TEM characterizations of an individual particle at different orientations relative to the electron beam. When the tilting angle of the sample holder was increased from 0° to 50° , the profile of the nanosheet marked by a red circle gradually evolved from a rectangular rod to a plate, corresponding to the side and top views of the nanosheet, respectively. Furthermore, the atomic-resolution scanning transmission electron microscopy (STEM) image taken from the cross-section indicated that the nanosheet was only comprised of 8–10 at. layers (see Fig. S1).

To resolve the crystal structure, synchrotron powder X-ray diffraction (XRD) pattern was collected from the as-obtained sample and shown in Fig. 1c. Clearly, the reflections are completely different from those expected for face-centred cubic (*fcc*) and hexagonal close-packed (*hcp*) Rh [30,40]. Indexing of the XRD pattern resulted in a unique space group of *Pmnn*, which belongs to an orthorhombic lattice. To confirm this assignment and obtain detailed crystallographic

information, Rietveld refinement was conducted against the diffraction patterns using a model with four Rh and two C atoms in the unit cell (inset of Fig. 1a). Fig. 1c and Table S1 show the results. The simulated and experimental diffraction patterns are consistent with each other, giving a satisfying goodness-of-fit (GOF) value ($R_{\rm wp}=3.1$ %). The refined lattice parameters are a = 3.074(6) Å, b = 4.779(4) Å, and c = 4.745(0) Å, respectively. The fractional coordinates of Rh atom are 0, 0.339(7), 0.252(0), with the C atoms filling half of the octahedral sites (see Table S1). Due to the much weaker X-ray scattering power of C relative to Rh, even the most prominent C-related diffraction peak (1.88 Å⁻¹ in Fig. 1c) appeared to be very weak in the XRD pattern. Therefore, we also acquired neutron diffraction patterns and low-frequency Raman spectra from the same batch of sample. Fig. 1d shows the results of Rietveld refinement against the neutron diffraction data using the model derived from the XRD pattern and the results agree well with the experimental data ($R_{\rm wp}=1.4$ %). Raman shifts corresponding to the lattice vibrations of orthorhombic RhCx were also

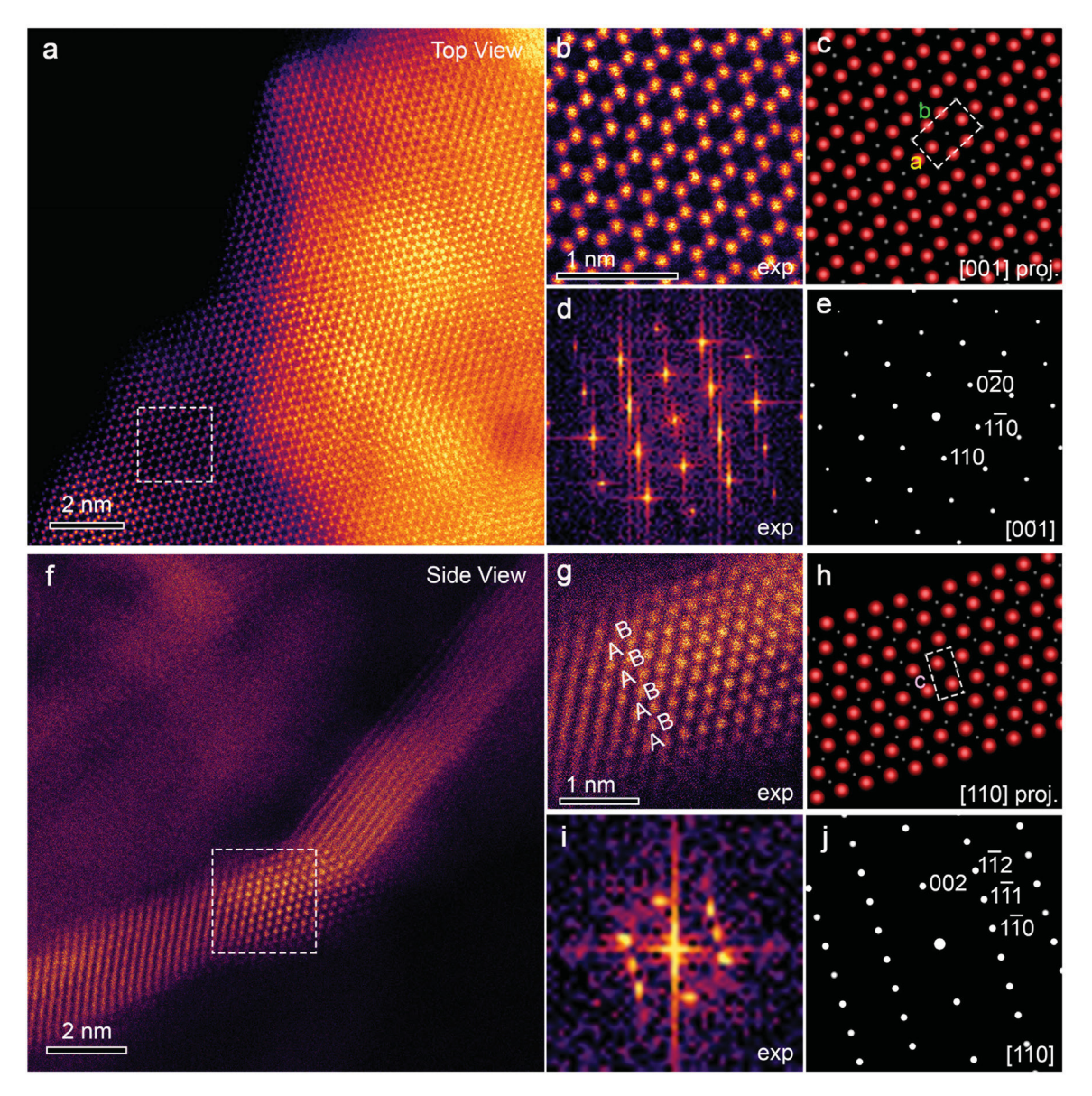


Fig. 2. (a) Aberration-corrected STEM image of an RhC $_x$ nanosheet viewed from the top surface. (b) Atomic-resolution STEM image taken from the region marked in (a). (c) Crystal structure projected along [001] zone axis based on the orthorhombic structure. (d) FFT image of the selected area marked in (a). (e) Diffraction pattern projected along the [001] zone axis of the orthorhombic structure. (f) Aberration-corrected STEM image of the RhC $_x$ nanosheet viewed from the side. (g) Atomic-resolution STEM image taken from the area marked in (f). (h) Crystal structure projected along the [110] zone axis of the orthorhombic structure. (i) FFT image of the selected area marked in (f). (j) Diffraction pattern projected along the [110] zone axis of the orthorhombic structure.

observed in the low-frequency region at 90.7 and 198.2 cm⁻¹ (see the Fig. S2), confirming the existence of C atoms in the Rh lattice.

To further validate the crystal structure, aberration-corrected STEM images were taken along different zone axes and then used to derive the FFT patterns. Fig. 2a shows a top-view STEM image, where the outline of a single nanosheet can be clearly resolved. Atomic-resolution STEM image of the area selected in Fig. 2a and the corresponding FFT pattern are shown in Figs. 2b and 2d, respectively. Regular and periodic arrangement of Rh atoms could be well resolved, indicating that each nanosheet was a single crystal. Figs. 2c and 2e, respectively, show the simulated atomic packing and diffraction pattern along the [001] zone axis based on the orthorhombic structure. The experimental and simulated results matched with each other, providing additional evidence to support the proposed crystal structure. Based on the STEM image (Fig. 2b) and simulated diffraction pattern (Fig. 2e), the exposed basal planes of the nanosheet could be indexed as {001}. In addition, the angles between two adjacent edges of the nanosheet were fixed at 115° (Fig. S3), consistent with the angle between {110} facets. As such, the side face of the nanosheet could be assigned to {110}. When the electron beam is aligned parallel to the nanosheet, as illustrated in Fig. 2f and g, the atomic stacking can be described as ABABAB along the direction perpendicular to the nanosheet. Based on the simulated atomic packing along the [110] zone axis of an orthorhombic lattice in Fig. 2h, the arrangement of atomic layers along < 001 > direction is also ABABAB. Combining with the XRD, neutron diffraction, Raman spectroscopy, and atomic-resolution STEM data, we can conclude that the RhC_x nanosheets are crystalized in an orthorhombic phase rather than the highly symmetric fcc or hcp structure upon the insertion of C atoms.

It should be noted that although the atomic stacking along <0001> direction in an hcp structure is also ABABAB [40,41], there are major differences between the orthorhombic and hcp phases. As shown in Figs. 2b and 2c, unlike the Rh atoms in an hcp structure, the six Rh atoms are not arranged into a regular hexagon. The interplanar spacing along a and b axes also increase by 14.3 % and 2.6 %, respectively (Fig. S4). Further evidence can be found in the FFT and diffraction patterns in Figs. 2d and 2e. The angle between $0\overline{2}0$ and $1\overline{1}0$ is 57.25° , different from the angle of 60° for an hcp structure. Furthermore, the density of the RhC_x is only 10.43 g·cm⁻³, much lower than that of Rh in the closest packing (12.46 g·cm⁻³). This difference implies significant lattice expansion for the orthorhombic phase when compared with the hcp structure characterized by a similar but closer atom packing.

2.2. Catalytic selectivity of the RhCx nanosheets toward C-C cleavage

With C atoms situated at well-controlled positions of the lattice and the presence of a well-defined surface structure, the RhCx nanosheets can serve as a model system to examine the effect of interstitial C atoms on catalysis. We chose to focus on the ethanol oxidation reaction (EOR) for its important role in DEFCs, a promising power source for mobile electronic devices, but its development still being limited by the inefficient selectivity for the C-C bond cleavage [42-46]. Breaking the C-C bond means total oxidation of ethanol to CO2 and transfer of 12 electrons to achieve the highest efficiency. In comparison, the formation of side products such as acetaldehyde and acetic acid only involves 2 and 4 electrons, respectively, and it is difficult to further oxidize acetic acid under common anode conditions [36-39]. To acquire a better selectivity, tunability of the electronic structure of catalysts based on the change of d-band centre to modulate the chemisorption energy of the reaction intermediates, namely a moderate binding strength for CO, CH_x, and acetyl or acetaldehyde, but higher energy for OH binding, has been widely adopted through the surface-structure control and/or alloying of noble metal nanocrystals [38]. Herein, to acquire a detailed mechanism about the effect of interstitial C atoms, the RhCx nanosheets and their Rh counterpart that adopted an identical morphology but without C atoms in the lattice (fcc phase, together with {111} facets on

the surface, see Fig. S5) were compared for their electrocatalytic activity toward EOR in terms of C-C cleavage.

Fig. 3a compares the cyclic voltammograms (CVs) of the two catalysts recorded in N_2 -saturated 1.0 M NaOH solutions. The shape and potentials of H adsorption/desorption on the RhCx nanosheets were different from those on the reference catalyst, likely due to their difference in surface structure. Fig. 3b shows the positive scan CV curves of EOR in N_2 -saturated solutions containing 1.0 M NaOH and 1.0 M ethanol at a scan rate of 50 mV·s⁻¹. As shown in Fig. 3c, the RhC_x nanosheets exhibited higher mass activity at 253.6 mA·mg⁻¹, which was 3.1 as high as that of the Rh counterpart (81.2 mA·mg⁻¹). Same tendency can be also found for the specific activity normalized by the electrochemical surface area (obtained from H adsorption/desorption), where RhC_x nanosheets outperformed the Rh counterpart with 1.9 times better activity. Besides, the onset potential of the RhCx was lower than the reference catalyst, demonstrating the improvement in kinetics for EOR. Further analysis of the CV curves, considerable differences can be clearly found in terms of the peak feature, where the two peaks at -0.24 V and - 0.09 V for Rh counterpart (dash line in Fig. 3b) merged into one peak at - 0.21 V for RhC_x nanosheets (solid line in Fig. 3b), suggesting their major difference in selectivity toward EOR [47].

To gain insights into the difference, in situ Fourier transform infrared (FTIR) reflection spectra were collected during EOR. Figs. 3d and 3e show the FTIR spectra collected from the two catalysts at potentials varying from - 0.8 V to 0 V at an interval of 0.1 V. In the spectra, the two upward bands at 1045 cm⁻¹ and 1085 cm⁻¹ can be attributed to the C-O stretching modes of ethanol [48]. The two strong downward peaks at 1551 cm⁻¹ and 1414 cm⁻¹ can be ascribed to the asymmetric and symmetric stretching modes, respectively, of the O-C-O unit in acetate ion (CH₃COO⁻) [38,49]. The band that shifted from 1800 cm⁻¹ to 1836 cm⁻¹ with the variation in potential can be assigned to the bridge-adsorbed COad species (COB) and the band in the range of 2035-2042 cm⁻¹ corresponds to the C-O band of the linearly adsorbed CO_{ad} species (CO_L) [50,51]. It is expected that CO₂, the product of the complete oxidation of ethanol, would react with OH to form carbonate (CO_3^{2-}) in an alkaline solution. The corresponding IR band of CO_3^{2-} (1390 cm⁻¹) tends to overlap with the acetate band at 1414 cm⁻¹, resulting in a stronger intensity at 1414 cm⁻¹ than that at 1551 cm⁻¹. As illustrated in Figs. 3d and 3e, the difference in peak intensity at $1414\ cm^{-1}$ and $1551\ cm^{-1}$ for the RhCx nanosheets were much greater than that of the Rh counterpart, suggesting a greater selectivity toward CO2 formation on the RhCx phase. We also measured the selectivity by applying a quantitative analytical IR method to determine the relative concentration (C_R) of the products of EOR (Figs. S6-S8) [48,52]. As shown in Fig. 3f, the RhCx nanosheets displayed greater selectivity toward CO₂ in the potential region from - 0.40 V to 0 V, together with higher catalytic activity. Specifically, the CO_2 selectivity at 0 V on the RhC_x nanosheets was about 18.1 %, much greater than that of the Rh counterpart (10.0 %), as well as the values previously reported for Rh (110) [45], Rh(100) [30], and monometallic Pt (1-7.5 %) and Pd (2.5 %) at room temperature [31,48,49,52]. These results highlight the great electrocatalytic performance of the RhCx nanosheets, especially the ability to cleave the C-C bond of ethanol during EOR. Besides the determination of the selectivity, peak assignment for the CV curves can be also conducted with the help of in situ FTIR spectra. Three peaks located at -0.45 V, -0.24 V and -0.09 V (dashed lines in Fig. 3b) can be clearly distinguished. The peak around - 0.45 V corresponds to the formation of CO, while the second and third peaks at about -0.24 V and - 0.09 V can be attributed to the formation of acetic acid and CO₂. This is consistent with the previous conclusion that CO is the main product at lower potential scope while acetic acid and CO2 formed at higher potential [47]. In the case of RhC_x, the second and third peaks merged into one peak at -0.21 V, which may result from the higher selectivity toward CO₂ compared with the Rh counterpart.

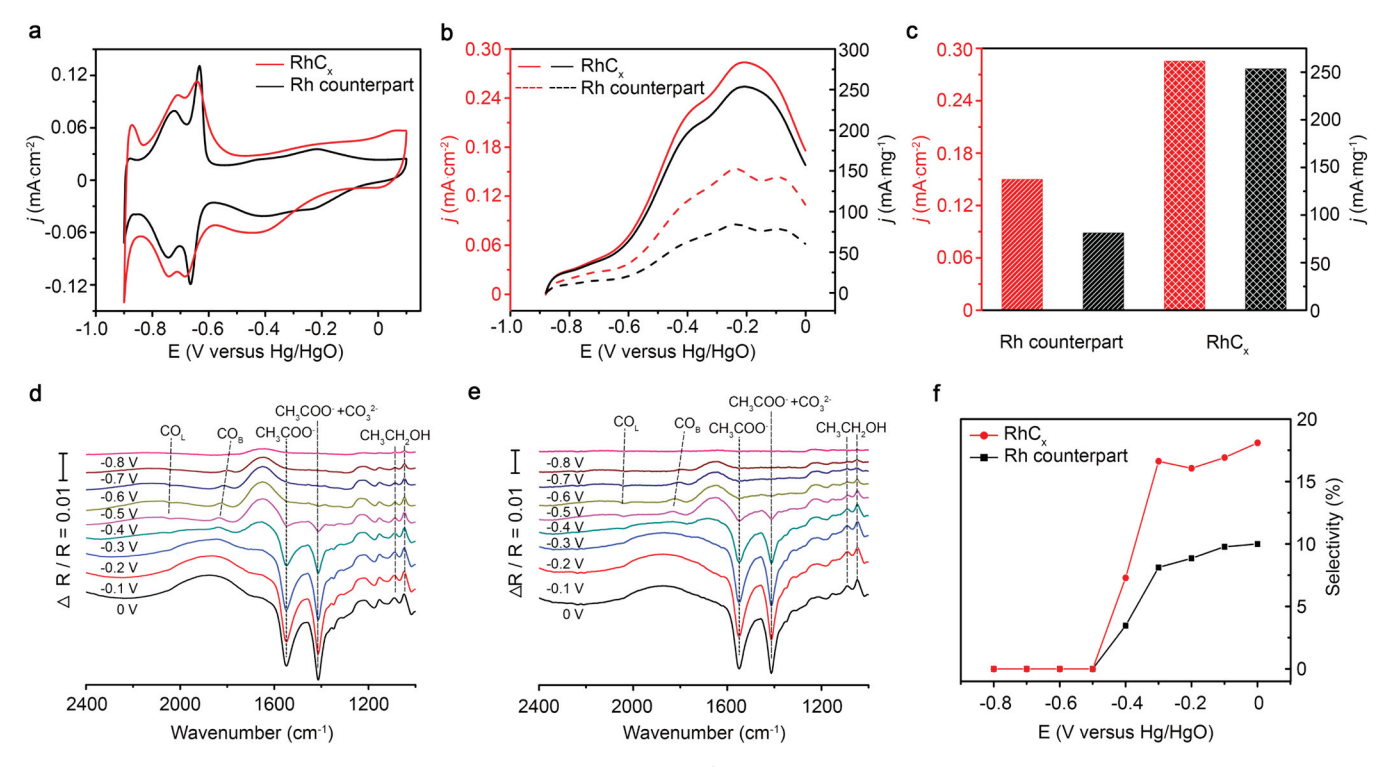


Fig. 3. (a) CV curves in N_2 -saturated solutions of 1.0 M NaOH (scan rate: 50 mV·s⁻¹). (b) Positive-scan CV curves in N_2 -saturated solutions containing 1.0 M NaOH and 1.0 M ethanol (scan rate: 50 mV·s⁻¹). (c) Catalytic activity of the different catalysts toward EOR. (d) and (e) *In situ* FTIR spectra of (d) the RhC_x nanosheets and (e) the Rh counterpart at different potentials in solutions containing 1.0 M NaOH and 1.0 M ethanol, E_S was varied from -0.80-0 V, $E_R = -0.90$ V, 200 scans, and the resolution was 8 cm⁻¹. (f) Potential dependence of the selectivity for the complete oxidation of ethanol to CO_2 (actually, carbonate in a highly alkaline solution).

2.3. Effect of lattice C atoms on C-C cleavage

To understand the high selectivity of RhC_x nanosheets toward C-C cleavage, theoretical calculations were performed to elucidate the

mechanism of ethanol dissociation. We calculated and compared the possible elemental steps by density functional theory (DFT), including the C-H activation, C-C cleavage, and coupling with OH*. The energetically-favored reaction pathway for ethanol dissociation on

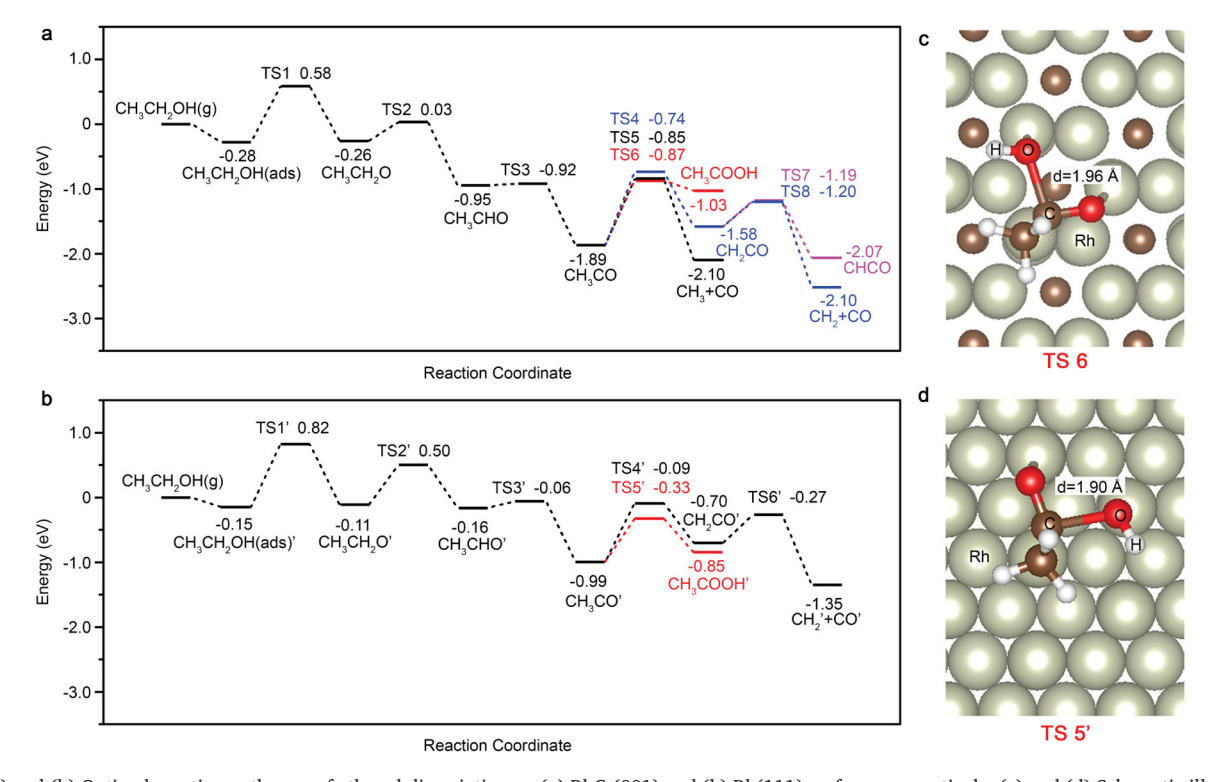


Fig. 4. (a) and (b) Optimal reaction pathways of ethanol dissociation on (a) $RhC_x(001)$ and (b) Rh(111) surfaces, respectively. (c) and (d) Schematic illustration of the transition structures of CH_3CO^* and OH^* on (d) Rh(111) and (e) $RhC_x(001)$ surfaces, respectively.

 $RhC_x(001)$ surface is shown in Fig. 4a. The initial step of ethanol activation on $RhC_x(001)$ is the cleavage of O-H bond to produce $CH_3CH_2O^*$ intermediate, which has the lowest overall dehydrogenation barrier compared to those pathways involving other initial dehydrogenation process C_{α} -H and C_{β} -H, as shown in Fig. S9. Then, the $CH_3CH_2O^*$ intermediate undergoes sequential dehydrogenation steps to form CH_xCO^* species, which are the precursors for the C-C bond cleavage. The relevant structures of intermediates and transition states (TS) are presented in Fig. S10.

We also investigated ethanol dissociation on Rh(111) surface, as shown in Fig. 4b [45]. The favorable reaction pathways for ethanol dissociation on RhCx(001) and Rh(111) are almost identical. However, the dehydrogenation barrier on RhC_x(001) surface is lower than that on Rh(111), resulting in a higher activity on RhC_x(001). For the selectivity toward CO2, on the one hand, the barrier to C-C bond breaking of CH₂CO* species on RhC_x(001) is lower than that on Rh(111), 0.38 eV vs. 0.43 eV. More importantly, the CH₃CO* species can easily couple with OH* on Rh(111) to form the dominating by-product CH₃COOH with a lower barrier (0.66 eV), rather than further dehydrogenating to form CH₂CO* (0.90 eV). In comparison, this coupling step can be effectively suppressed on RhC_x(001) due to a higher barrier of 1.00 eV. Therefore, the RhC_x(001) surface exhibits a higher selectivity toward CO₂, which is consistent with the experimental results. In addition, the dehydrogenation to CH2CO* and C-C cleavage to CH3* and CO are more exothermic compared with the coupling reaction to CH3COOH on RhC_x(001) surface, in favor of higher selectivity for the breaking of C-C bond.

To further elucidate the relationship between the coupling reaction barrier and crystal structure at the molecular level, zoomed-in images of TS on RhC_x(001) and Rh(111) were analysed and their corresponding barriers were decomposed as well. Here a co-adsorption model was adopted to analyse the so-called reactant-activation energy that represents the energy cost for CH₃CO* (OH*) moving from initial states (IS) to TS in the absence of OH* (CH₃CO*) [53,54]. The calculation details and corresponding values of all terms are respectively specified in Fig. S11 and Table S2. The reactant-activation energies of CH_3CO^* (ΔE_{CH3CO^*}) on two different surfaces are quite similar, while it is much harder for another reactant OH* to move from IS to TS on RhC_x(001) than that on Rh(111). As such, the difference in barrier to the coupling reaction is mainly determined by the difference in reactant-activation energy of OH^* (ΔE_{OH^*}). Therefore, we further analysed the *Bader* charge of O on OH-adsorbed RhC_x(001) and Rh(111) surfaces, shown in Table S3. A much greater extent of electron transfer from the metal to the adsorbed OH on RhC_x(001) was found, indicating a stronger bond between OH and $RhC_x(001)$ surface than that on Rh(111). In other words, much more energy is necessary for the activation of OH* to couple with CH3CO* on RhC_x(001). Typically, the difference in reactant-activation energy is mainly determined by the variation in electronic structure for the metal surface. Hence, we calculated the density of states (DOS) of the two different surfaces, as shown in Fig. S12. The DOS of RhCx(001) and Rh (111) are rather different in terms of shape and energy range. The projected DOS of Rh atoms on $RhC_x(001)$ is distributed much broader than that on Rh(111) due to the insertion of C atoms, where a large overlap between the d orbitals of Rh and the p orbitals of C can be identified in the ranges of $-4.13\,\text{eV}$ to $-7.33\,\text{eV}$ and $0.24\,\text{eV}$ to 3.38 eV. If Rh atoms adopt the same orthorhombic structure but without C atoms (expressed as ortho-Rh(001), shown in Fig. S12c), the d orbitals of Rh atoms are mainly distributed between - 4.13 eV and 1.66 eV, manifesting the significant effect of interstitial C atoms on the electronic structure of the catalyst surface. It is also validated by the results of X-ray photoelectron spectroscopy (XPS) and Bader charge of Rh in RhC_x(001), confirming the charge transfer between C and Rh atoms (Fig. S13 and Table S3).

Beside the difference in reactant-activation energy, there are also some distinctions about the interaction energy $\Delta E_{\rm int}$, which is highly related to the geometric structure of the metal surface. Figs. 4c and 4d

show the transition structures of CH_3CO^* and OH^* . Clearly, the OH* and CH_3CO^* species do not share the same metal atoms, the distance between the O atom of OH* and the carbonyl C atom in CH_3CO^* on Rh(111) is 1.90 Å, while it increased to 1.96 Å on $RhC_x(001)$. This suggested that the energy of TS on $RhC_x(001)$ would be higher than that on Rh(111), leading to a larger energy barrier to the coupling reaction on $RhC_x(001)$. The value of ΔE_{int} on $RhC_x(001)$ is 0.13 eV, larger than that on Rh(111) surface (0.03 eV), in agreement with the variation in geometric structure between the two different surfaces, where large lattice expansion was found on $RhC_x(001)$ because of the insertion of C atoms into the octahedral interstices.

2.4. Enhancing the catalytic properties of Rh black with interstitial C atoms

Based on the understanding of the catalytic effect of interstitial C atoms on Rh nanosheets, we also attempted to improve the performance of commercial Rh black. As shown in Fig. 5a and 5b, when treated in a mixture of oleylamine and formaldehyde, the commercial Rh black was partially transformed into the orthorhombic RhC_x phase. The interstitial C atoms only existed in the subsurface region. Generally, in contrast to the incorporation of C atoms during the growth of nanocrystals, namely the bottom-up approach [29], it is much more challenging to introduce these foreign atoms into the lattice of an existing crystal under mild conditions [28,55]. To the best of our knowledge, this is the first report on the insertion of C atoms into the lattice of preformed nanocrystals through a mild wet chemical approach. When benchmarked against the pristine Rh black, the as-modified Rh black (orthorhombic RhCx) exhibited 2.5- and 1.9-times improvement in selectivity and specific activity, respectively, as shown in Figs. 5c, 5d and Fig. S14. In addition, the stability test of the modified commercial Rh black was carried out through the long-term chronoamperometric method recorded at -0.3 V(vs Hg/HgO). With periodic activation in fresh 1.0 M NaOH solution, the activity can be fully recovered, shown in Fig. S15a. Besides, the CV curves of the initial and final states of the modified commercial Rh black were similar (Fig. S15b), but significantly different from the pristine commercial Rh black with fcc structure. This suggests that the orthorhombic RhCx structure was stable during the chronoamperometric stability test. These observations not only further validate the remarkable effect of interstitial C atoms but also hold great promise for enhancing the performance of industrial catalysts.

3. Conclusion

In summary, we have successfully introduced C atoms into the interstitial sites of well-defined Rh nanosheets and further elucidated the electronic and geometric effects of the C atoms on the C-C cleavage during ethanol electrooxidation at the molecular level. With the incorporation of C atoms, the Rh lattice changed from the highly symmetric cubic structure to an orthorhombic phase, with the added C atoms occupying half of the distorted octahedral sites. The electron transfer between C and Rh atoms, as well as the expanded crystal lattice, reduced the barrier to dehydrogenation step and increased the barriers to side reactions, leading to enhancement in both selectivity and activity. More importantly, the insights on structural transition and catalytic mechanism were further utilized to directly introduce C atoms into the subsurface region of commercial Rh black to greatly enhance its catalytic selectivity and activity toward ethanol oxidation.

CRediT authorship contribution statement

Zhenming Cao: Conceptualization, Methodology, Investigation, Writing – original draft, Writing – review & editing. Huiqi Li: Conceptualization, Methodology, Investigation, Writing – original draft, Writing – review & editing. Yunchao Sun: Investigation. Cong Shen: Investigation. Yaqi Jiang: Writing – review & editing. Qiyuan Fan:

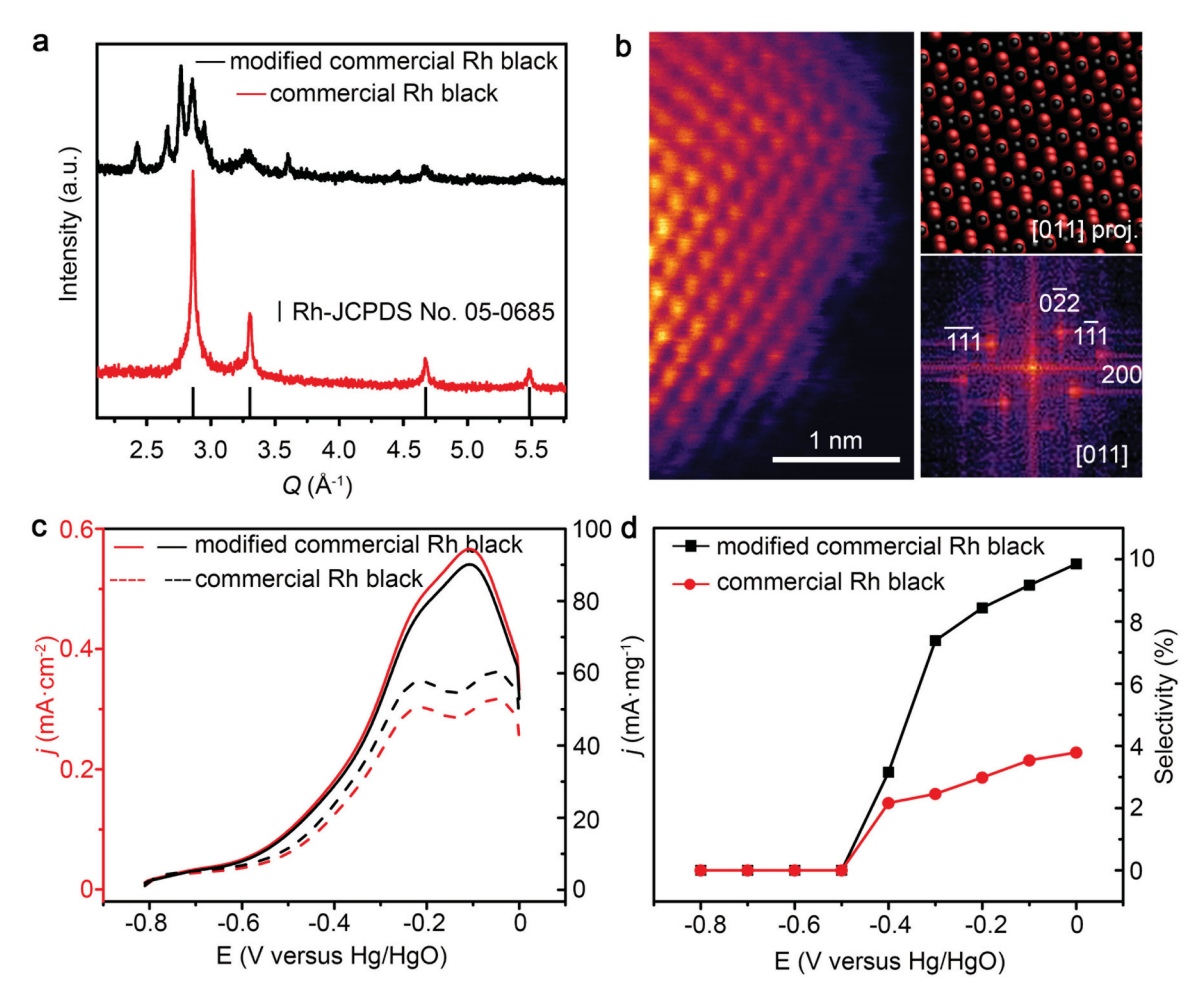


Fig. 5. (a) XRD patterns of a commercial Rh black before and after treatment in a mixture of oleylamine and formaldehyde at 200 $^{\circ}$ C for 12 h. (b) Atomic-resolution STEM image, crystal structure projected along [011] zone axis and FFT image of the post treated commercial Rh black. (c) Positive-scan CV curves in a N₂-saturated solution containing 1.0 M NaOH and 1.0 M ethanol (scan rate: 50 mV·s⁻¹). (d) Potential dependence of the selectivity for the complete oxidation of ethanol to CO₂.

Formal analysis. Jun Cheng: Formal analysis, Writing – review & editing. Zhantao Liu: Investigation. Hailong Chen: Investigation, Writing – review & editing. Zitao Chen: Investigation. Miaofang Chi: Investigation, Writing – review & editing. Jinyu Ye: Investigation. Maofeng Cao: Investigation. Zhaoxiong Xie: Writing – original draft, Writing – review & editing, Project administration, Funding acquisition. Younan Xia: Supervision.

Declaration of Competing Interest

The authors declare that they have no known competing financial interests or personal relationships that could have appeared to influence the work reported in this paper.

Data availability

Data will be made available on request.

Acknowledgements

This work was supported by the National Key Research and Development Program of China (2020YFB1505802), and the Natural Science Foundation of China (No. 21931009, 21721001). Part of the research was conducted at Georgia Tech under the partial support by the start-up funds from Georgia Tech while Zhenming Cao was a visiting graduate student in the Xia Group. Hailong Chen and Zhantao Liu acknowledge the financial support from the NSF (DMR 2004878). Part of the electron

microscopy analyses was performed at the Oak Ridge National Laboratory's Centre for Nanophase Materials Sciences, which is a Department of Energy, Office of Science User Facility. Use of the Advanced Photon Source at Argonne National Laboratory was supported by the U. S. DOE, Office of Science, Office of Basic Energy Sciences, under Contract No. DE-AC02-06CH11357. A portion of this research used resources at the Spallation Neutron Source, a DOE Office of Science User Facility operated by the Oak Ridge National Laboratory.

Appendix A. Supporting information

Supplementary data associated with this article can be found in the online version at doi:10.1016/j.nanoen.2023.108597.

References

- D.I. Enache, J.K. Edwards, P. Landon, B. Solsona-Espriu, A.F. Carley, A.A. Herzing, M. Watanabe, C.J. Kiely, D.W. Knight, G.J. Hutchings, Science 311 (2006) 362–365
- [2] R.A. Sheldon, H. Van Bekkum, Fine Chemicals through Heterogeneous Catalysis, John Wiley & Sons, 2008.
- [3] G. Chen, C. Xu, X. Huang, J. Ye, L. Gu, G. Li, Z. Tang, B. Wu, H. Yang, Z. Zhao, Z. Zhou, G. Fu, N. Zheng, Nat. Mater. 15 (2016) 564–569.
- [4] P.P. Zhao, X.X. Sun, S. Hao, Y.H. Zhang, J.X. Chen, H. Zhang, S.J. Dong, ACS Energy Lett. 8 (2023) 1697–1704.
- [5] L. Lin, W. Zhou, R. Gao, S. Yao, X. Zhang, W. Xu, S. Zheng, Z. Jiang, Q. Yu, Y.-W. Li, C. Shi, X.-D. Wen, D. Ma, Nature 544 (2017) 80–83.
- [6] Y. Guo, X.B. Yang, X.C. Liu, X.L. Tong, N.J. Yang, Adv. Funct. Mater. 33 (2023) 2209134–2209145.

- [7] R. Ye, J. Zhao, B.B. Wickemeyer, F.D. Toste, G.A. Somorjai, Nat. Catal. 1 (2018)
- [8] G. Ertl, H. Knözinger, F. Schüth, J. Weitkamp. Handbook of Heterogeneous Catalysis, VCH Verlag GmbH & Co. KGaA, Weinheim, Germany, 2008.
- [9] Y. Shi, Z. Lyu, M. Zhao, R. Chen, Q.N. Nguyen, Y. Xia, Chem. Rev. 121 (2021) 649-735.
- [10] Z.X. Ge, T.J. Wang, Y. Ding, S.B. Yin, F.M. Li, P. Chen, Y. Chen, Adv. Energy Mater. 12 (2022) 2103916–2103927.
- M. Cargnello, V.V. Doan-Nguyen, T.R. Gordon, R.E. Diaz, E.A. Stach, R.J. Gorte, P. Fornasiero, C.B. Murray, Science 341 (2013) 771–773.
- [12] S.T. Marshall, M. O'Brien, B. Oetter, A. Corpuz, R.M. Richards, D.K. Schwartz, J. W. Medlin, Nat. Mater. 9 (2010) 853–858.
- Y. Jia, Y. Jiang, J. Zhang, L. Zhang, Q. Chen, Z. Xie, L. Zheng, J. Am. Chem. Soc. 136 (2014) 3748–3751.
- [14] T. Altantzis, I. Lobato, A. De Backer, A. Béché, Y. Zhang, S. Basak, M. Porcu, Q. Xu, A. Sánchez-Iglesias, L.M. Liz-Marzán, G. Van Tendeloo, S. Van Aert, S. Bals, Nano Lett 19 (2019) 477-481
- [15] S.H. Pang, C.A. Schoenbaum, D.K. Schwartz, J.W. Medlin, Nat. Commun. 4 (2013) 2448–2454.
- T.Y. Chen, C. Foo, S.C.E. Tsang, Chem. Sci. 12 (2022) 517-532.
- J.Y. Wang, Y.Y. Kang, H. Yang, W.B. Cai, J. Phys. Chem. C 113 (2009) 8366-8372.
- [18] S.M. Davis, F. Zaera, G.A. Somorjai, J. Catal. 77 (1982) 439-459.
- [19] Detre Teschner, J.ános Borsodi, Attila Wootsch, Zsolt Révay, Michael Hävecker, Axel Knop-Gericke, S. David Jackson, R. Schlögl, Science 320 (2008) 86–89.

 [20] R. Guo, Q. Chen, X. Li, Y. Liu, C. Wang, W. Bi, C. Zhao, Y. Guo, M. Jin, J. Mater.
- Chem. A 7 (2019) 4714–4720.
- [21] O. Piqué, I.Z. Koleva, F. Viñes, H.A. Aleksandrov, G.N. Vayssilov, F. Illas, Angew. Chem. Int. Ed. 58 (2019) 1744-1748.
- Y. Sun, Y. Cao, L. Wang, X. Mu, Q. Zhao, R. Si, X. Zhu, S. Chen, B. Zhang, D. Chen, Y. Wan, Nat. Commun. 11 (2020) 4600–4609. [22]
- Y. Wang, B. Liu, X. Lan, T. Wang, ACS Catal. 11 (2021) 10257-10266. **[23]**
- [24] S.B. Ziemecki, G.A. Jones, D.G. Swartzfager, R.L. Harlow, J. Faber Jr., J. Am. Chem. Soc. 107 (1985) 4547-4548.
- [25] F. Viñes, C. Loschen, F. Illas, K.M. Neyman, J. Catal. 266 (2009) 59-63.
- N. Seriani, F. Mittendorfer, G. Kresse, J. Chem. Phys. 132 (2010) 024711–024720.
- [27] R. Schuster, M. Bertram, H. Runge, S. Geile, S. Chung, V. Vonk, H. Noei, A. Poulain, Y. Lykhach, A. Stierle, J. Libuda, Phys. Chem. Chem. Phys. 23 (2021) 1371–1380.
- [28] S. Ono, T. Kikegawa, Y. Ohishi, Solid State Commun. 133 (2005) 55–59.
- [29] T. Wakisaka, K. Kusada, D. Wu, T. Yamamoto, T. Toriyama, S. Matsumura, H. Akiba, O. Yamamuro, K. Ikeda, T. Otomo, N. Palina, Y. Chen, L.S.R. Kumara, C. Song, O. Sakata, W. Xie, M. Koyama, Y. Kubota, S. Kawaguchi, R.L. Arevalo, S. M. Aspera, E.F. Arguelles, H. Nakanishi, H. Kitagawa, J. Am. Chem. Soc. 142 (2020) 1247-1253.
- [30] J. Zhang, J. Ye, Q. Fan, Y. Jiang, Y. Zhu, H. Li, Z. Cao, Q. Kuang, J. Cheng, J. Zheng, Z. Xie, J. Am. Chem. Soc. 140 (2018) 11232-11240.
- [31] C. Bianchini, P.K. Shen, Chem. Rev. 109 (2009) 4183-4206.
- [32] R. Kavanagh, X.-M. Cao, W.-F. Lin, C. Hardacre, P. Hu, Angew. Chem. Int. Ed. 51 (2012) 1572-1575.
- [33] A. Pei, G. Li, L. Zhu, Z. Huang, J. Ye, Y.-C. Chang, S.M. Osman, C.-W. Pao, Q. Gao, B.H. Chen, R. Luque, Adv. Funct. Mater. 32 (2022) 2208587-2208599.
- [34] H. Wang, H. Zheng, L. Ling, Q. Fang, L. Jiao, L. Zheng, Y. Qin, Z. Luo, W. Gu, W. Song, C. Zhu, ACS Nano 16 (2022) 21266-21274.
- [35] R. Wu, L. Wang, Phys. Chem. Chem. Phys. 25 (2023) 2190–2202.
 [36] B. Lan, Q.L. Wang, Z.X. Ma, Y.J. Wu, X.L. Jiang, W.S. Jia, C.X. Zhou, Y.Y. Yang, Appl. Catal. B Environ. 300 (2023) 120728–120735.
- [37] Y. Wei, Z. Mao, X.-Y. Ma, C. Zhan, W.-B. Cai, J. Phys. Chem. Lett. 13 (2022) 11288-11294.
- Y. Wang, S.Z. Zou, W.B. Cai, Catalysts 5 (2015) 1507-1534.
- H.-F. Wang, Z.-P. Liu, J. Am. Chem. Soc. 130 (2008) 10996-11004.
- J.L. Huang, Z. Li, H.H. Duan, Z.Y. Cheng, Y.D. Li, J. Zhu, R. Yu, J. Am. Chem. Soc. 139 (2017) 575–578. [40]
- Z. Cao, Q. Chen, J. Zhang, H. Li, Y. Jiang, S. Shen, G. Fu, B.A. Lu, Z. Xie, L. Zheng, [41] Nat. Commun. 8 (2017) 15131-15138.
- [42] A. Kowal, M. Li, M. Shao, K. Sasaki, M.B. Vukmirovic, J. Zhang, N.S. Marinkovic, P. Liu, A.I. Frenkel, R.R. Adzic, Nat. Mater. 8 (2009) 325–330.
- [43] K. Liu, W. Wang, P. Guo, J. Ye, Y. Wang, P. Li, Z. Lyu, Y. Geng, M. Liu, S. Xie, Adv. Funct. Mater. 29 (2019) 1806300–1806309. [44] R. Rizo, R.M. Aran-Ais, E. Padgett, D.A. Muller, M.J. Lazaro, J. Solla-Gullon, J.
- M. Feliu, E. Pastor, H.D. Abruna, J. Am. Chem. Soc. 140 (2018) 3791-3797. [45] H.Q. Li, Q.Y. Fan, J.Y. Ye, Z.M. Cao, Z.F. Ma, Y.Q. Jiang, J.W. Zhang, J. Cheng, Z.
- X. Xie, L.S. Zheng, Mater. Today Energy 11 (2019) 120–127.
- P. Wang, H. Cui, C.X. Wang, Nano Energy 66 (2019) 104196–104204. C. Zhu, B. Lan, R.-L. Wei, C.-N. Wang, Y.-Y. Yang, ACS Catal. 9 (2019) 4046–4053. [47]
- Z.Y. Zhou, Q.A. Wang, J.L. Lin, N. Tian, S.G. Sun, Electrochim. Acta 55 (2010) [48] 7995–7999.
- [49] P.A. Christensen, S.W.M. Jones, A. Hamnett, J. Phys. Chem. C 116 (2012) 24681-24689.
- [50] Y.Y. Yang, J. Ren, Q.X. Li, Z.Y. Zhou, S.G. Sun, W.B. Cai, ACS Catal. 4 (2014) 798-803
- [51] J.Y. Ye, Y.X. Jiang, T. Sheng, S.G. Sun, Nano Energy 29 (2016) 414-427.
- [52] Z.Y. Zhou, D.J. Chen, H. Li, Q. Wang, S.G. Sun, J. Phys. Chem. C 112 (2008)
- Z.-P. Liu, P. Hu, J. Am. Chem. Soc. 125 (2003) 1958-1967.
- [54] Z.-P. Liu, P. Hu, J. Chem. Phys. 115 (2001) 4977–4980.
- E. Gregoryanz, C. Sanloup, M. Somayazulu, J. Badro, G. Fiquet, H.-K. Mao, R. J. Hemley, Nat. Mater. 3 (2004) 294–297. [55]



Zhenming Cao received his B.S. from the University of Jinan in 2012 and acquired the Ph.D. at Xiamen University with Prof. Zhaoxiong Xie. As a jointly supervised student, he joined Younan Xia's group from 2017 to 2019. He is currently a postdoctoral scholar co-guided by Prof. Xueqian Kong and Xiaogang Peng at Zhejiang University. His current research interest focuses on the chemical doping and oxidation of infrared quantum dots.



Huiqi Li received her B.S. degree from the Department of Chemistry at Heilongjiang University in 2015. She continued her academic pursuits and completed her Ph. D. degree in the Department of Chemistry and Chemical Energineering at Xiamen University under the supervision of Prof. Zhaoxiong Xie in 2021. Her current research focuses on the controlled synthesis of nanocrystals for small molecular oxidation and oxidation reduction reaction in alkaline fuel cells.



Oi-Yuan Fan received her Ph.D. degree in 2020 at Xiamen University under the supervision of Prof. Jun Cheng. She then continued to work as a postdoctoral researcher at Xiamen University in the group of Prof. Cheng. Since 2022, she joined the School of Chemistry and Chemical Engineering, Shanxi University, where she currently holds a position as a lecturer. Her research interests are mainly focused on simulating the dynamic process of heterogeneous catalysis using ab initio



Zhantao Liu is currently a Postdoctoral scholar researcher in Dr. Hailong Chen's group at Georgia Institute of Technology. Prior to that, he received his B.S., M.S., and P.hD. from Beihang University, Hong Kong University of Science and Technology and Georgia Institute of Technology. His research mainly focuses on solid-state electrolytes and solid-state batteries.



Zitao Chen received his B.S. and Ph.D. from South China University of Technology in 2014, 2020 respectively. During 2017-2019, he worked on electron microscopy at Georgia Tech and Oak Ridge National Laboratory as visiting student. Since 2021. Chen has been a Post-Doc in Institute of Physics. Chinese Academy of Science. His current research interests are understanding the behavior of amorphous material at atomic scale by employing electron tomography and spectroscopy.



Yunchao Sun received his BSc degree in chemistry from Heilongjiang University in 2019. He received his master's degree under the supervision of Assoc. Prof. Yaqi Jiang and Prof. Zhaoxiong Xie in 2022. His research focuses on the development of Rh- and Pd-based nanocrystals with controllable morphology and electrochemical catalytic properties.



Miaofang Chi is a distinguished scientist at the Center for Nanophase Materials Sciences in Oak Ridge National Laboratory (ORNL). She received her master's degree at the Shanghai Institute of Ceramics (Chinese Academy of Sciences) and completed her doctoral research in materials science at the University of California, Davis. In 2008, Chi joined ORNL, where she develops and applies microscopy techniques into materials for energy and sustainability. Her primary research interests are understanding interfacial charge transfer and mass transport behavior in energy and quantum materials and systems by advancing and employing novel electron microscopy techniques.



Jin-Yu Ye received his Ph.D. degree from Department of chemistry of Xiamen University in 2016 under the supervision of Prof. Shi-Gang Sun. He is currently an engineer of chemistry at Xiamen University. His research interests include surface electrochemistry, electrocatalysis and Spectro electrochemistry.



Jun Cheng graduated in Chemistry at Shanghai Jiao Tong University, China. He received his Ph.D. degree in 2008 at Queen's University, Belfast. He then moved to the University of Cambridge as a postdoctoral researcher. From 2010–2013, Cheng has been a junior research fellow at Emmanuel College at Cambridge. Since 2013, he has been a lecturer at the Department of Chemistry, University of Aberdeen. In 2005, he joined the College of Chemistry and Chemical Engineering, Xiamen University, China, where he has remained, holding the position of professor since then. His current research interests include computational electrochemistry, theoretical catalysis, and machine-learning-based simulation.



Mao-Feng Cao completed his Bachelors in Materials Chemistry at East China University of Science and Technology, China, in 2018. Now He joined Prof. Bin Ren's group at Xiamen University, China, for his Ph.D. degree. His research focuses on ultra-low-frequency Raman spectroscopy, tip-enhanced Raman spectroscopy and their applications in two-dimensional materials.



Hailong Chen is an Assistant Professor of the Woodruff School of Mechanical Engineering at Georgia Institute of Technology. He received his B.S. and M.S. from Tsinghua University and Ph. D. from Stony Brook University. His research interests include design of novel electrode materials for Li-ion and Na-ion batteries and solid-state electrolytes with using combined computational and experimental approaches. His research also focuses on the development of in situ X-ray structural characterization techniques.



Cong Shen received her B.S. degree from Tiangong University in 2018. Then she continued to pursue her Ph.D. degree at Xiamen University. Her research interest is the controllable synthesis and assembly of nanomaterials.



Zhaoxiong Xie received his B.S., M. S., and Ph.D. degrees from department of chemistry, Xiamen University in 1987, 1990 and 1995, respectively. Since 2002, he has held the position of Professor of physical chemistry at Xiamen University. He won the National Distinguished Young Scientist Fund of China in 2007 and Chang Jiang Chair Professorship in 2014. His current research interests are focused on surface/interfacial chemistry of functional inorganic nanomaterials.



Yaqi Jiang received her BSc degree (1986), MSc degree (1989) and Ph.D. degree (2011) from the Department of Chemistry at Shanghai Jiao Tong University, Fuzhou University and Xiamen University, respectively. She has been an associate professor of physical chemistry at Xiamen University since 2004. Her current research interest mainly focuses on the structure-activity relationship of noble-metal based nanomaterials.



Younan Xia received his Ph.D. in Physical Chemistry from Harvard University in 1996 with George M. Whitesides. He started as an Assistant Professor of Chemistry at the University of Washington (Seattle) in 1997 and then joined the Department of Biomedical Engineering at Washington University in St. Louis in 2007 as the James M. McKelvey Professor. Since 2012, he has held the position of Brock Family Chair and GRA Eminent Scholar in Nanomedicine at the Georgia Institute of Technology. He has served as an Associate Editor of Nano Letters since 2002.